PCIM Europe 2017; International Exhibition and Conference for Power Electronics, Intelligent Motion, Renewable Energy and Energy Management; Proceedings of

Medium Frequency Transformer Design and Optimization

M. Mogorovic and D. Dujic

POWER ELECTRONICS LABORATORY
ÉCOLE POLYTECHNIQUE FÉDÉRALE DE LAUSANNE

Medium Frequency Transformer Design and Optimization

Marko Mogorovic, Drazen Dujic
Power Electronics Laboratory, École Polytechnique Fédérale de Lausanne (EPFL), Switzerland
marko.mogorovic@epfl.ch, drazen.dujic@epfl.ch

Abstract

This paper describes the technical challenges tied to modeling and design optimization of the medium frequency transformer (MFT) for power electronic applications, namely emerging solid state transformers (SSTs). A detailed analysis and modeling of the phenomena governing the MFT electrical behavior as well as limiting the operation and design range is performed. A synthesis of all these models is done in form of a design optimization algorithm capable of generating the set of all feasible transformer designs. Moreover, design filters are developed allowing to search for the most preferable design alternatives in terms of hot-spot temperatures, weight, volume and efficiency. Finally, a full scale MFT prototype has been realized according to the optimal specifications outputted by the proposed design optimization tool.

1. Introduction

With the proliferation of power electronic semiconductor switches for high power, the notion of substituting the traditional line frequency power transformers (LFT) in MV distribution grids and on-board traction applications with the system consisting of much smaller and lighter MFTs driven by power electronic converters, namely the solid state transformer (SST), has been gaining popularity [1]. This solution is especially interesting for on-board traction supplies operated at $16.7Hz$ line frequency as the decrease in transformer weight and volume are both most drastic and the most important design criteria for these applications. Despite the increased worldwide research effort, the SST technology is still on a level of academic and advanced industry prototypes [2].

While the LFT is one of the oldest and well established technologies in the field of electrical engineering, high-power high-voltage MFT is not yet a fully mature or standardized technology. There exists plenty of area for improvements in terms of modeling, insulation coordination, electrical parameter control, thermal coordination and the overall design optimization. In the documented research on modeling and design optimization of the MFT [3]–[5], the design considerations tied to the proper insulation coordination are usually neglected and there is no information about any insulation testing (e.g. PD and BIL tests). Furthermore, besides the discussion, selection and application of the available analytical sub-system models (e.g. leakage inductance [6], core [7]–[9] and winding losses [10]–[20]), from the often quite old literature, there has not been much effort directed into improving the accuracy and precision of these estimations.

Designing a high-power high-voltage medium frequency transformer is associated with multiple technical challenges related to electrical, magnetic, dielectric and thermal performance limits encountered in the system. Various technological choices must be carefully considered and selected before being included into a generic multi-objective optimization. Moreover, the quality of the result of the optimization is only as good as the utilized models. Therefore, all relevant phenomena, within physical subsystems of this complex multi-physical system, must be modeled both accurately and precisely in reference to their impact on the given application. Especially, precise control of electric parameters is paramount when it comes to the design of the MFT for resonant converters where the transformer is a part of a resonant circuit. Finally, the problems of correct insulation and thermal coordination and choice of the technologies involved in the transformer design itself still remain under discussion.

This paper discusses the main considerations and provides a complete design optimization process of an MFT, together with full experimental verification on a realized $100kW$ prototype.

ISBN 978-3-8007-4424-4

2. MFT Design Optimization

While it is tempting to perform the MFT design optimization utilizing some of the available and formal mathematical optimization tools, the highly nonlinear and non-convex nature of the problem and a mix of continuous and discrete variables makes this a rather difficult task. Moreover, proper setting of the multi-variable objective function in order to select the desired design is neither straight forward nor intuitive. Instead, we have chosen to rely on a very primitive yet, in this particular case, very reliable brute-force approach supplemented with certain considerations allowing the algorithm to exclude many of the designs which test infeasible in the preliminary check. This lowers the computational weight and increases the capacity of the algorithm in terms of the initial design space size.

The proposed MFT optimization algorithm consists of two stages. The main structure of the brute-force optimization used in each stage with certain modifications is displayed in Fig. 1. This algorithm adopts all the good features of the proposed design optimization techniques available in literature [3]–[5] and uses them in combination. Furthermore, it allows more degrees of freedom in terms of geometrical design considerations that have been overlooked, thus enabling the algorithm to generate a more diverse population of designs uncovering the otherwise neglected design possibilities. This is enabled using a transformation of the problem that decreases the number of the optimization variables, e.g. by treating the whole winding as a single object instead of an array of turns.

The algorithm takes the available data-sheet inputs, electrical and dielectric references and optimization variables ranges (primary number of turns, current densities, litz wire strand AWG and normalized geometrical proportions). The "prepare data" function generates the optimization space where each optimization variable vector variation corresponds to a fully defined single design. Winding losses and magnetic energy are calculated using [6] and dielectric distance between the windings is calculated to match the reference leakage inductance based on the magnetic energy calculation. Air gap is cal-

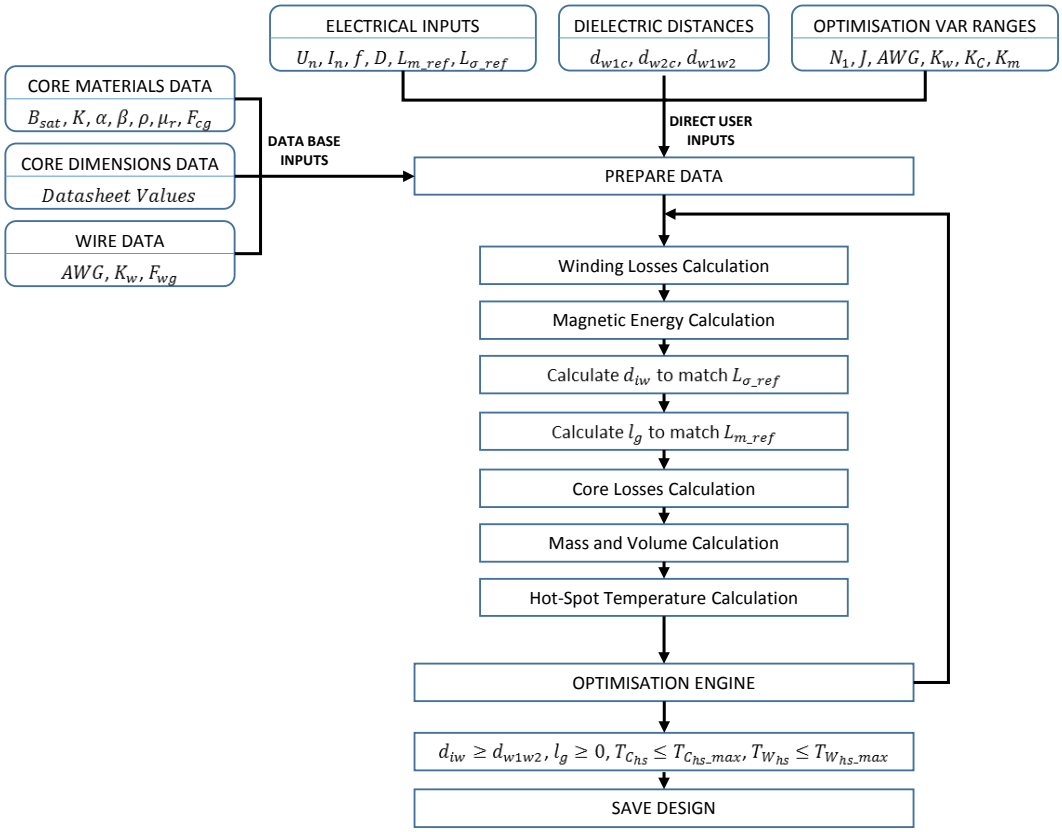

Fig. 1: Brute force MFT design optimization algorithm

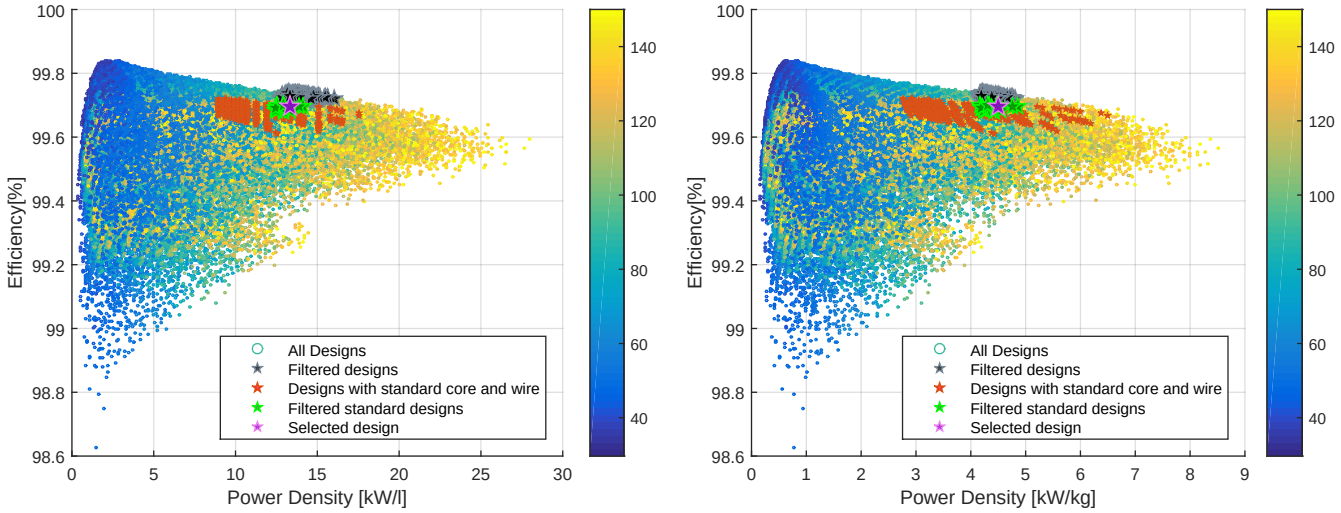

Fig. 2: Plot of all possible MFT designs (around two million designs) and filtered optimal designs according to specifications from Table 1: (a) Efficiency vs. volume power density (b) Efficiency vs. weight power density

Tab. 1: MFT prototype reference electric specifications

P_n	$100kW$	V_1	$750V$	$L_{\sigma1}, L_{\sigma2}$	$3.27\mu H$
f_{sw}	$10kHz$	V_2	$750V$	L_m	$1.8\mu H$

culated to match the magnetization inductance reference. Core losses [7], mass and volume calculation is performed and finally the hot-spot temperatures are generated utilizing the developed thermal model (not discussed in this paper). Each design that passes the feasibility check is saved into a design database.

Another novelty of the proposed methodology lies in the data post processing treatment. In the first stage of the optimization, all of the optimization variables are varied freely and thus all the mathematically feasible designs are exposed, as displayed with circle markers in Fig. 2 where the color code corresponds to the highest hot-spot temperature within the windings. These designs are then filtered in terms of key performance indicators (e.g. efficiency, weight, volume, hot-spot temperature margins etc.), as highlighted with black star markers. The filtered designs are then analyzed against available standard core and wire geometries and the most similar components are selected. The design is re-optimized with fixed discrete values of standard core and wire geometries and the results are displayed relative to all possible solutions in Fig. 2 with red star markers. The user defined performance filters are again applied on the design database with standard designs (green star markers) and the final design is selected from this set, based on the construction simplicity or other metric (purple star marker).

This method does not only bridge the gap between the theoretical solutions and the ones that can be made out of the standard components, but it also provides an insight into where the solution utilizing which of the available hardware are positioned relative to all possible theoretical designs in an intuitive way.

Having a full set of all possible solutions, provided by the brute force algorithm, allows to analyze all different design alternatives in an arbitrarily narrowed down design space, depending on the set filters. This makes the selection of the optimal solution much easier and more intuitive compared to the analysis of one or multiple sets of Pareto-optimal solutions as would be the case with formal optimization algorithms.

The most popular Pareto front, related to the trade-off between efficiency and power density, is exposed at the upper edges of the feasibility sets of the plots in Fig. 2. Its descending trend shows how the price in efficiency must be paid in order to achieve a smaller design solution.

ISBN 978-3-8007-4424-4

3. MFT Prototype

Applying the described optimization process to a transformer with electric specifications shown in Table 1, an optimal MFT design is selected, as displayed in Fig. 2. The realized prototype is an air insulated and air cooled shell type MFT featuring square litz wire windings and N87 SIFERRIT cores.

The 3D CAD models are created in SOLIDWORKS, according to the optimal design specifications generated by the optimization algorithm. Primary and secondary winding each consist of eight turns of the square profiled (8.7x$8.7 \pm 0.2mm$) copper litz wire with $1400\ AWG\ 32$ litz strands and a total copper crossection of $43.96mm^2$, wound on the corresponding coil formers, as displayed in Fig. 3a. The primary and secondary coil formers have been produced using additive manufacturing process (3D printing) out of PA2200 high strength thermally resistant plastic. They have been designed and optimized in 3D SOLIDWORKS both to maximize the mechanical support strength and area for natural convective air cooling of the windings with respect to the mechanical properties of the selected wire, as displayed in Fig. 3b. The MFT core is made of 48 (12 x 4) SIFERRITE U-cores (UU9316 - CF139).

The realized $100kW$ MFT prototype is displayed in Fig. 3c. Even though the prototype is almost identical as the 3D CAD design, there exist a couple of small (measured in parts of mm) differences in the geometry due to the precision limitations of the technological assembly process and material imperfections which effect the electric parameters of the MFT.

Due to the brittle nature of ferrite materials and manufacturing tolerances in terms of the surfaces and dimensions, mechanical amortization is necessary at every surface of contact with another solid material. Due to this effect, there is a significant difference between the reference magnetizing inductance from Table 1 and the one that was measured on the MFT prototype ($L_m = 750\mu F$) as the width of the interfacing pad maintaining the air-gap distance had to be chosen larger than calculated due to mentioned mechanical constraints.

On the other hand, bending of the large cross-section litz wire is not a simple task and relatively large bending radiuses, that are hard to achieve in the corner regions of the winding, need to be considered in order to limit the bulging and twisting effect of the wire. Consequently, there exists an offset in the winding placement of around $1mm$ compared to the 3D CAD. Furthermore, the wire itself has a slightly larger profile than stated in the data sheet. Consequently, the H field distribution in the window area and the leakage inductance is effected. As a result, the measured leakage inductance ($L_{\sigma 1} = L_{\sigma 2} = 4.2\mu H$) is higher than the reference value from Table 1.

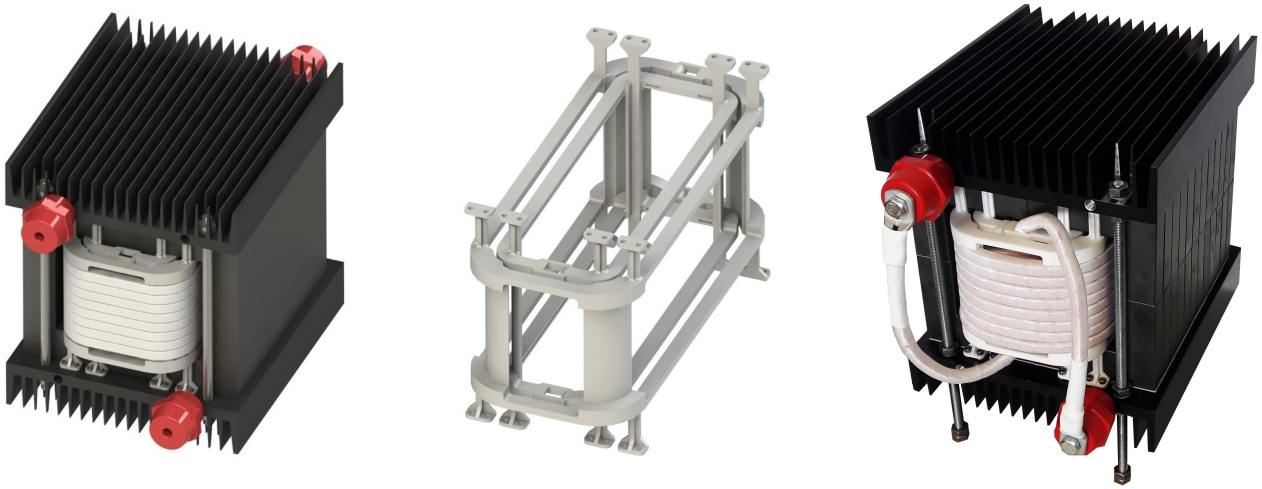

(a) (b) (c)

Fig. 3: Optimal design resulting from the optimization algorithm: (a) MFT 3D CAD render (b) Primary and secondary coil formers 3D CAD render (c) Realized MFT prototype

ISBN 978-3-8007-4424-4

4. Experimental Verification

4.1. Dielectric Withstand Test

In order to verify the achieved insulation level, the MFT prototype was tested in a high voltage test setup displayed in Fig. 5, normally used for AC dielectric withstand and partial discharge tests. The tests were carried by applying the voltage: i) between the primary and the secondary winding; ii) between the secondary winding and the conductive parts of the MFT (top and the bottom heatsinks and the vertical studs). The critical partial discharge level ($10pC$) has been recorded at $4kV$, applied between the primary and the secondary windings. Due to mechanical imperfections of the MFT prototype, insulation level is slightly lower than expected.

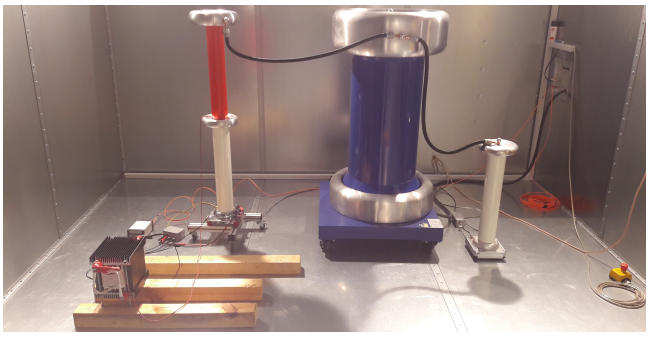

Fig. 5: MFT dielectric withstand test

4.2. Resonant Test Setup

In order to carry out the electrical tests on the MFT prototype, a full power rated resonant test setup was assembled. The electrical scheme of the test setup and its physical layout inside the protective cage are displayed in Fig. 4 and Fig. 6, respectively.

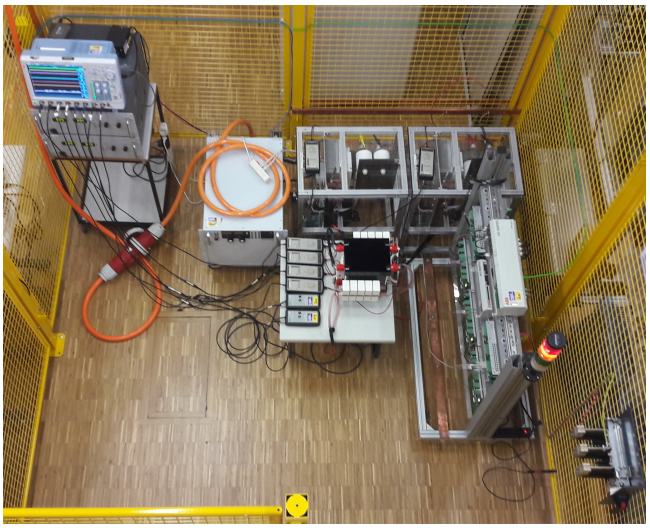

Fig. 6: Layout of the test setup within the protective cage

The setup consists of two H-bridge modules, one actively switched and the other operating as a diode rectifier, with their corresponding DC-bus capacitors, the resonant tank comprised of the MFT and the distributed resonant capacitors (C_{r1} and C_{r2}) and two DC sources, one operated in voltage (U_{DC1}) and the other in current (I_{DC}) control mode. The setup is operated as a resonant converter at the constant frequency $f_{sw} = 10kHz$ and with the constant duty cycle $D = 0.5$. Positive ends of the DC-buses on the primary and secondary side are short circuited, whereas their negative ends are connected through a current source (I_{DC}) thus allowing the circulation of the energy from the secondary side back to the primary side DC-bus, as displayed in Fig. 4.

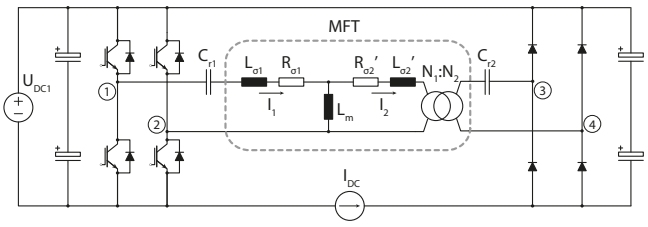

Fig. 4: Electrical scheme of the test setup

The two H-bridges are physically realized by utilizing two phases of two three-phase SEMIKRON Skiip modules, as displayed in Fig. 6. The one on the primary side is actively controlled via the optical PWM signals generated using the ABB AC 800PEC high performance controller with control functions programmed graphically in MATLAB Simulink using real-time code generation.

Both primary (C_{r1}) and secondary (C_{r2}) capacitor of the distributed resonant capacitor bank are realized as a parallel connection of eight (7x5μF + 1x2.5μF) AC film capacitors, held by bus-bars, giving a total resonant tank capacitance of $18.75\mu F$ and consequently the resonant tank frequency of $f_0 = 12.7kHz$. Therefore, the desired sub-resonant con-

ISBN 978-3-8007-4424-4

verter operation is achieved, providing soft switching turn-on for the primary side switches and zero current switching for the secondary side diodes.

All devices within the protective test cage, two DC sources, 8-channel oscilloscope, and AC 800PEC controller, as displayed in Fig. 6, are connected through their ethernet connection to the multi-port active switch communicating with the PC via the optical cable thus ensuring safety and complete electrical decoupling of the operator from the high power test setup.

Voltages on the AC side of the H-bridge converter (U_{12}) and the diode rectifier (U_{23}) are measured together with the resonant capacitor voltages on both the primary (U_{Cr1}) and secondary (U_{Cr2}) side, as well as the primary (I_1) and secondary (I_2) resonant currents. Furthermore, the DC-bus voltages on each Skiip module, and the output AC currents of the two converters are measured with additional sensors and used to implement safety features (e.g. over-voltage and over-current protection) within the controller software. Voltages and currents of both DC sources are monitored to evaluate the power injected into the test setup, covering the total losses during the operation. Temperature on the outer surfaces of the MFT are monitored with a laser thermal sensor to detect any dangerous overheating.

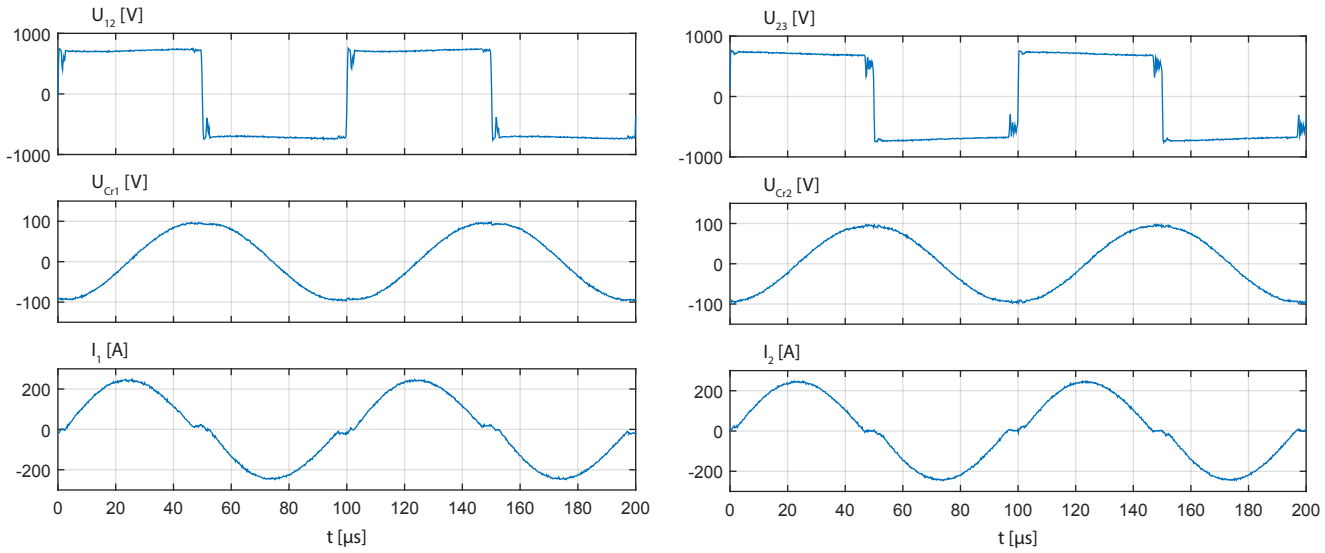

(a) (b)

Fig. 7: Measured waveforms on the primary (a) and secondary (b) MFT side at nominal power: voltages on the inputs of the resonant tank (top), voltages on the resonant capacitors (middle) and resonant currents (bottom)

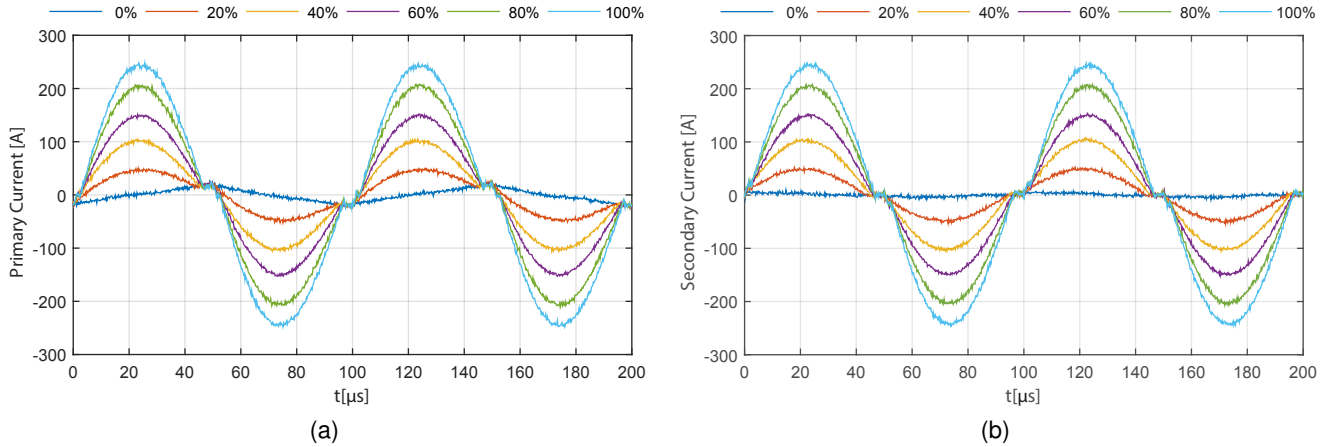

(a) (b)

Fig. 8: Measured current waveforms on the primary (a) and secondary (b) side of the MFT at different loading conditions in range from 0% to 100% of the rated power

ISBN 978-3-8007-4424-4

4.3. Measurements

The measured voltage and current waveforms, from the primary and secondary side of the MFT at nominal power operation, are displayed in Fig. 7a and Fig. 7b, respectively. Top plots show the voltage waveforms on the output of the H-Bridge (U_{12}) and the input of the diode rectifier (U_{34}). Primary side voltage is regulated by DC voltage source U_{DC1} to $750V$. Middle plots show the voltages on the primary (U_{Cr1}) and secondary (U_{Cr2}) side resonant capacitors. Bottom plots show the primary (I_1) and secondary (I_2) resonant current waveforms. One can observe that resonant tank current and capacitor voltage are in quadrature, without any distortion, indicating well balanced operation. Resonant current plots show that the resonant frequency corresponds to the calculated value (f_0) and that the sub-resonant switching is achieved as one of the main conditions for soft switching operation. The maximum switch-off current of the IGBTs is therefore limited by the peak value of the magnetization current ($I_{m_{max}} = 25A$).

Plots of the primary and secondary resonant currents, under various loading conditions ranging from 0% to 100% of the rated power, are displayed in Fig. 8a and Fig. 8b, respectively. Under no-load conditions, only the magnetizing current is present in the circuit. As the power transfer is increased, typical resonant waveform is established with rms value proportional to the operating power level.

Due to inability to reduce the dead time below the $3\mu s$ set by the gate driver, it can be observed from Fig. 7 that a minor and incomplete loss of the zero voltage switching occurs at $100kW$ operating point. This was not a major concern during MFT testing, considering that the resonant test setup was of sufficient ratings, and the objective of the paper is not on the converter optimization.

Total losses of the whole resonant test setup can be calculated from the voltage and current readings on the two DC power supplies U_{DC1} and I_{DC}. The total power injected into the setup at the nominal power was measured as $2.9kW$, indicating the overall resonant converter efficiency of 97.1%. This is a reasonable result, taking into account that, with the exception of the MFT, the setup was not optimized for the given operation.

On the other hand, it is hard to accurately separate the losses using data from the conducted tests, thus making the exact estimation of the MFT efficiency difficult. However, by calculating the semiconductor losses in the setup, considering well defined operating conditions, they account to $2.2kW$ (this does not include DC link and resonant capacitor losses). Thus, the MFT efficiency can be estimated to be above 99.3% at rated operating conditions.

5. Conclusions

A complete, brute force based, MFT design optimization process, relying on detailed analytical modeling has been presented. Due to the lack of space, improved leakage inductance calculation and thermal model, develop by authors are not presented in detail and will be documented in future publications. The results of the application of the proposed design procedure on a specific MFT design requirements, have been illustrated and analyzed in detail, exposing various design trade-offs that must be carefully considered. While the design tool can develop, analyze and compare large number of designs (e.g. several hundred of thousands to couple of millions), ultimate selection of a design is left to the user, who is greatly assisted with developed filters, allowing easy and intuitive navigation through a design space.

To verify utilized modeling approaches and effectiveness of the design process, a $100kW$ rated MFT prototype has been realized, using the standard off-the-shelf components, based on the design specifications generated by the algorithm. Despite the best effort by the authors, mechanical imperfections and limitations of the integration process, have resulted in slight deviation of some electrical parameters, providing useful feedback for improvements of robustness of the optimization process.

Realized MFT prototype has been successfully tested at various operating resonant conditions. Test results have confirmed electrical performance in accordance with design specifications, achieving high efficiency without any thermal issues. Therefore, the developed design optimization procedure was successfully verified, proving its usefulness and providing assurance for future designs.

ISBN 978-3-8007-4424-4

References

[1] J. E. Huber and J. W. Kolar, "Solid-State Transformers: On the Origins and Evolution of Key Concepts," *IEEE Industrial Electronics Magazine*, 10, no., pp. 19–28, Sep. 2016.

[2] M. Claessens, D. Dujic, F. Canales, J. K. Steinke, P. Stefanutti, and C. Vetterli, "Traction Transformation: A Power-Electronic Traction Transformer (PETT)," *ABB Review, No: 1/12*, no., pp. 11–17, 2012.

[3] I. Villar, "Multiphysical Characterization of Medium-Frequency Power Electronic Transformers," PhD thesis, EPFL Lausanne, Switzerland, 2010.

[4] G. Ortiz, "High-Power DC-DC Converter Technologies for Smart Grid and Traction Applications," PhD thesis, ETH Zurich, Switzerland, 2014.

[5] M. Bahmani, "Design and Optimization Considerations of Medium-Frequency Power Transformers in High-Power DC-DC Applications," PhD thesis, Chalmers University of Technology Gothenburg, Sweden, 2016.

[6] P. L. Dowell, "Effects of eddy currents in transformer windings," *Proceedings of the Institution of Electrical Engineers*, 113, no., pp. 1387–1394, Aug. 1966.

[7] K. Venkatachalam, C. Sullivan, T. Abdallah, and H. Tacca, "Accurate prediction of ferrite core loss with nonsinusoidal waveforms using only Steinmetz parameters," no., pp. 36–41, Jun. 2002.

[8] J. Reinert, A. Brockmeyer, and R. De Doncker, "Calculation of losses in ferro- and ferrimagnetic materials based on the modified Steinmetz equation," *IEEE Transactions on Industry Applications*, 37, no., pp. 1055–1061, Jul. 2001.

[9] D. Lin, P. Zhou, W. Fu, Z. Badics, and Z. Cendes, "A dynamic core loss model for soft ferromagnetic and power ferrite materials in transient finite element analysis," *IEEE Transactions on Magnetics*, 40, no., pp. 1318–1321, Mar. 2004.

[10] C.R. Sullivan, "Optimal choice for number of strands in a litz-wire transformer winding," *IEEE Transactions on Power Electronics*, 14, no., pp. 283–291, Mar. 1999.

[11] R. W. Erickson and D. Maksimovic, *Fundamentals of Power Electronics*, en. Springer US, Jan. 2001.

[12] F. Tourkhani and P. Viarouge, "Accurate analytical model of winding losses in round Litz wire windings," *IEEE Transactions on Magnetics*, 37, no., pp. 538–543, Jan. 2001.

[13] G. S. Dimitrakakis, E. C. Tatakis, and E. J. Rikos, "A new model for the determination of copper losses in transformer windings with arbitrary conductor distribution under high frequency sinusoidal excitation," no., pp. 1–10, Sep. 2007.

[14] A. Stadler, "The optimization of high frequency inductors with litz-wire windings," no., pp. 209–213, Jun. 2013.

[15] J.G. Breslin and W.G. Hurley, "Computer aided high frequency transformer design using an optimized methodology," no., pp. 277–280, 2000.

[16] W.G. Hurley, E. Gath, and J. Breslin, "Optimizing the AC resistance of multilayer transformer windings with arbitrary current waveforms," *IEEE Transactions on Power Electronics*, 15, no., pp. 369–376, Mar. 2000.

[17] P. Thummala, H. Schneider, Z. Zhang, Z. Ouyang, A. Knott, and M. A. E. Andersen, "Efficiency Optimization by Considering the High-Voltage Flyback Transformer Parasitics Using an Automatic Winding Layout Technique," *IEEE Transactions on Power Electronics*, 30, no., pp. 5755–5768, Oct. 2015.

[18] C. R. Sullivan, T. Abdallah, and T. Fujiwara, "Optimization of a flyback transformer winding considering two-dimensional field effects, cost and loss," 1, no., 116–122 vol.1, 2001.

[19] J. G. Breslin and W. G. Hurley, "Derivation of optimum winding thickness for duty cycle modulated current waveshapes," 1, no., 655–661 vol.1, Jun. 1997.

[20] R. P. Wojda and M. K. Kazimierczuk, "Winding resistance of litz-wire and multi-strand inductors," *IET Power Electronics*, 5, no., pp. 257–268, Feb. 2012.

ISBN 978-3-8007-4424-4